# Source Separation for Wideband Energy Emissions Using Complex Independent Component Analysis

L. R. Arnaut and C. S. Obiekezie

***Abstract*—Complex independent component analysis is formulated for ultrawideband (UWB) incoherent fields, based on maximum-likelihood estimation with iterative natural gradient searching. It can be applied to measurements of complex power separated in contributions by propagating and reactive near-fields. A set of novel nonlinear asymmetric score functions is derived that are asymptotically matched to skewed probability density functions of incoherent energy sources departing from ideal chi-square ensemble distributions. The source decomposition is applied to two analog and digital integrated circuits. Based on the measured intensity of the emitted magnetic field, the technique is shown to enable nonlinear extraction of a set of independent spatially separated UWB sources, without knowledge of neither the detailed circuit geometry nor its on-board signals. Overcompleteness of the data set is found to have a relatively small effect on the accuracy of the estimated magnitude and location of the emission hot spots, but has a major influence on the global spatial maps and nature of the extracted sources.**

***Index Terms*—Blind deconvolution, blind source separation, complex independent component analysis, electromagnetic interference, maximum-likelihood estimation (MLE), radiated emissions.**

## I. Introduction

ADVANCES in submicron lithography and use of new materials allow for complete systems nowadays to be built on a single ULSI chip. These fast-switching digital circuits and multiuser communication protocols, particularly spread-spectrum techniques, produce ultra-wideband (UWB) voltage and current fluctuations at ever increasing clock frequencies. Miniaturization and shrinking wavelengths $\lambda = 2\pi/k$ cause circuit components of characteristic size $d$ to behave as unintentional distributed radiators when $\lambda \sim d$. Increased signal bandwidths $\Delta\omega$ decrease the correlation length $\ell \sim c/\Delta\omega$ and, hence, the field coherency. This causes spatiotemporal field variations to appear as quasi-random fluctuations. Thus, unintentional emissions of electromagnetic (EM) fields exhibit increasing complexity and irregularity in space-time-frequency.

A basic paradigm in electromagnetic compatibility (EMC) and other areas of EM source identification is the detection of dominant emitters and their root cause ("source of sources"). Scanning probes allow for direct albeit often coarse inspection of the local emitted near field (NF). Since the number of potential emitters is often orders of magnitude larger than the feasible number of scan points in measurements, the experimental determination of the on-board sources is an ill-posed inversion problem in the Hadamard sense (overcomplete or underdetermined system). Moreover, for UWB sources, their locations, orientations, amplitudes, phases, and correlations extracted using equivalent dipole modeling [1]–[3] should ideally be determined at each time instance or frequency. These characteristics may differ widely across frequency and do not necessarily coincide with those of the actual physical sources.

Stochastic techniques offer a powerful framework for identifying and separating UWB sources because increasing the number of observation frequencies *increases* the accuracy with which such sources can then be characterized and grouped. In [4], principal component analysis (PCA) was used to decorrelate and identify *dominant* emissions across the band. By decomposing a measured UWB field scan, spatial maps of *uncorrelated/orthogonal* basis fields (empirical eigenmodes) were extracted. PCA captures the bulk of the EM energy hierarchically in a small set of ranked principal components (PCs). However, as a pure field decomposition method (forward transformation), PCA does not enquire about the sources themselves. Also, if the measured field quantity is not Gaussian (e.g., using a square-law detector), then the extracted uncorrelated PCs are not necessarily independent nor maximally separated.

In this paper, we apply independent component analysis (ICA). This companion technique empirically extracts a set of maximally *independent* sources and their associated mixing (superposition) matrix between fields and sources using a nonorthogonal[1] decomposition in the source space. This extraction is achieved solely on the basis of measured field data. The mixing matrix can be related to the Green's dyadics for these sources if additional information on their constellation and polarization (purely geometric characteristics) is available. In line with usual conventions in statistics, deterministic and sample quantities will be denoted with lowercase Roman symbols, while uppercase letters refer to corresponding random variables.[2] Single, double, and triple underlined variables refer to

Manuscript received April 24, 2013; revised June 25, 2013 and October 29, 2013; accepted October 30, 2013. Date of publication January 1, 2014; date of current version May 19, 2014. This work was sponsored by the U.K. Engineering and Physics Research Council under contract no. EP/H051384/1. Health monitor device courtesy of Barrie Hayes-Gill of Monica Healthcare Ltd, U.K.

The authors are with the George Green Institute of Electromagnetics Research, University of Nottingham, Nottingham NG7 2RD, U.K. (e-mail: luk.arnaut@nottingham.ac.uk; eexcso@nottingham.ac.uk).

Color versions of one or more of the figures in this paper are available online at http://ieeexplore.ieee.org.

Digital Object Identifier 10.1109/TEMC.2013.2289384

[1]More precisely, ICA decomposition is merely orthogonal in the space of (linearly) decorrelated data. ICA performs a reorientation of eigenvectors in the PCA extracted subspace based on maximized independence as the optimality criterion. This is in contrast with varimax orthogonal rotation for PCA, which is based on maximization of residual variance. As a result, ICs are in general no longer mutually orthogonal, unlike PCs.

[2]Except for the numbers of observations $M$ and independent sources $N$, with $m$ and $n$ denoting their respective indices.

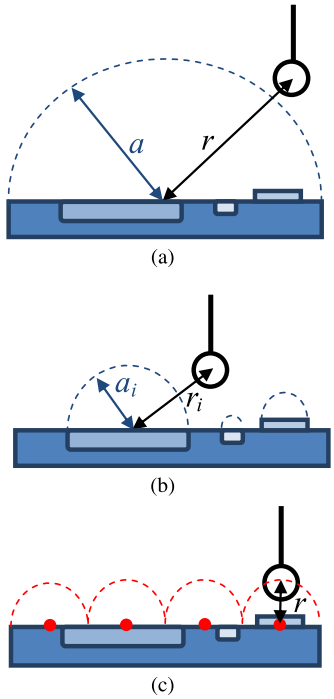


Fig. 1. Schematic diagram for circuit emissions. (a) Source region for coupled sources: encapsulating sphere of radius $a$ for entire circuit. (b) Source region for uncoupled sources: encapsulating spheres of radii $a_i$ for source $i$. (c) Scan distance for equivalent point dipole source ($a_i \to 0$), with MPE efficiency governed by $kr \gg 1$.

vectors, dyadics (matrices), and tryadics (third-order tensors). An $\exp(\mathrm{j}\omega t)$ dependence per frequency component is assumed and suppressed throughout. Throughout the paper, the shorthand term "independence" refers to statistical as opposed to functional independence.

## II. ICA of Random EM Fields and Their Sources

### A. Relevance

To appreciate the merit of separating unintentional emitters into mutually independent groups (clustered or entangled), consider the fact that these sources are often numerous, latent, intermittent, coupled, and that their root cause may be difficult to identify. This large number of degrees of freedom hampers accurate functional characterization of the source current density. Approximate representations of concentrated sources in terms of a multipole expansion (MPE) are then attractive. For a printed circuit board (PCB) viewed as a convex source, (exterior) MPE is possible only for field points at $\underline{r}$ outside a sphere of radius $a$ enclosing *all* sources [5], [6], i.e., containing the complete circuit ($r > a$) [see Fig. 1(a)]. Furthermore, MPE is practical only for electrically small sources ($ka \ll 1$) to ensure rapid series convergence and efficient representation by their first few MPE terms. For typical NF measurements, however, scan heights $r$ are required to be a mere fraction of the size of the circuit ($r \ll a$) to ensure adequate field resolution and SNR. If, now, the circuit can be represented as a set of *independent*, i.e., decoupled sources, then it can be partitioned into disjoint sources $i$, allowing for an exterior MPE of each individual source ($a_i \leq a$) [see Fig. 1(b)] followed by a superposition of these sources' emissions. Thus, separation into independent sources enables MPE for scan heights much closer to the circuit than without source partitioning ($a_i \leq a \Rightarrow r_i \leq r$). When representing these sources as point multipoles ($a_i \to 0$), only $\lambda$ but no longer $a_i$ serves as a metric for deciding on $r$ [see Fig. 1(c)]. Such source partitioning requires finding a set of noninteracting equivalent sources based on the mixed emitted fields.

Extraction of ICs is also fundamental in the rigorous stochastic characterization of random EM fields in static or dynamic systems when the number of degrees of freedom (independent samples) plays a crucial role [7]. This occurs, e.g., in sampling distributions or in *extreme value distributions* and their associated statistics and uncertainties for PCB emissions, reverberation chambers, etc. All of these require sets of *independent* (rather than merely uncorrelated) samples. For example, confidence intervals for the maximum emitted power $P_{\max}$ for time-varying signals are based on its cumulative distribution

$$F_{P_{\max}}(p_{\max}) = F_{P_1,P_2,\ldots,P_N}(p_1, p_2, \ldots, p_N) = \prod_{i=1}^{N} F_{P_i}(p_i = p_{\max}) = [F_{P_1}(p_1 = p_{\max})]^N \tag{1}$$

provided the $N$ samples, as "sources" for $P_{\max}$, are statistically independent. The latter equality in (1) applies provided the sources are, in addition, identically distributed.

### B. Independent Component Analysis

ICA is a purely data driven method of separating sources, without prior knowledge of specific characteristics of individual sources (i.e., locations, orientations, constellation, nor their amplitudes, phases, spectra, etc.), although some general basic assumptions are usually made [8]–[12]. To achieve such so-called blind separation, a field is measured under different parametric conditions producing a set of observations, from which their generating independent sources and their inverse transformation (called separation or decomposition matrix) are determined through linear superpositions of the measured fields. For linear ICA, the necessary and sufficient conditions for uniqueness and separability of the sources are that the sources be independent, nondegenerate, and that at most one source is Gaussian.[3] Each extracted independent component (IC) represents a set of mutually dependent emitting sources that is maximally independent of all other ICs, based on the observations. The extracted ICs are defined up to an arbitrary permutation (order) and complex scale factor (polarity, amplitude, and phase) [13]. Thus, ICA is unable to specify neither the strength of the extracted emitters nor their rank in their contribution to the resultant field. This ambiguity arises because ICA is an inverse transformation, in which the source vector and mixing matrix both need to be identified: the measured field only specifies their combined product.

[3]One circular Gaussian source or several Gaussian sources with mutually different circularity coefficients, in case of separability in complex ICA.

ICA offers a solution to the classical "cocktail party" problem of the unaided filtering of original messages in a received superposition of their signals. In [14] and [15], ICA was used as an electromagnetic interference diagnostic tool for estimating separate time series of multiple signals by analyzing crosstalk, which is a classical ICA application. Here, we show that ICA can also provide *spatial* separation of UWB sources.

### C. Problem Formulation

Consider the space-frequency distribution of a random EM field or field related quantity $\underline{X}(\underline{r},\omega)$ originating from $N$ primary or secondary sources, each one centered at $\underline{r}'_n$ $(n = 1,\ldots,N)$. In EMC, these sources are typically unknown and latent. They represent emitting passive or active circuit components, tracks, pins, vias, scatterers, etc. For a given configuration of their deterministic electric currents[4] $\underline{j}_n(\underline{r}'_n)$, the MPE of the field at an observation location point specified by $\underline{r}$ is [17]

$$\underline{x}(\underline{r}) = \sum_{n=1}^{N} \underline{\underline{g}}_{0n}(\underline{r}|\underline{r}'_n)\cdot\underline{p}_n(\underline{r}'_n) + \underline{\underline{g}}_{1n}(\underline{r}|\underline{r}'_n) : \underline{\underline{q}}_n(\underline{r}'_n) + \cdots \tag{2}$$

where $\underline{p}_n(\underline{r}'_n) \triangleq \int_{V'} \underline{j}_n dV'/(\mathrm{j}\omega)$, $\underline{\underline{q}}_n(\underline{r}'_n) \triangleq \int_{V'}(\underline{r}'\,\underline{j}_n + \underline{j}_n\,\underline{r}')dV'/(\mathrm{j}2\omega)$, etc., are the electric dipole, quadrupole, etc., moments of $\underline{j}_n(\underline{r}'_n)$. The electroelectric or magnetoelectric Green polyadics $\underline{\underline{g}}_{0n}$, $\underline{\underline{g}}_{1n}$, etc., are then deterministic and relate $\underline{x}(\underline{r})$ to the $n$th source (i.e., its 0th-order gradient), its first-order gradient, etc, respectively. Limiting (2) to local, i.e., dipole moment contributions, or grouping higher order multipole contributions into an equivalent *local* effect, the expansion can be rewritten compactly as

$$\underline{x} = \sum_{n=1}^{N} \underline{\underline{g}}_n \cdot \underline{p}_n, [\underline{x}] = \left[\underline{\underline{g}}\right]\cdot\left[\underline{p}\right] \tag{3}$$

where brackets denote vectorized, i.e., linear arrays for the specific constellation of fields and sources [18]. For unknown $\underline{j}_n(\underline{r}'_n)$, the problem is the identification of a sample set of $N$ statistically independent sources, $\underline{p} = [\underline{p}_n]$, based on $M$ independent observations of the field $\underline{x}_m(\underline{r}_m)$ $(m = 1,\ldots,M)$.[5] Since the locations, orientations, amplitudes, and phases of the sources are unknown but adjustable in order to yield an optimum solution $\{\underline{\underline{g}},\underline{p}\}$, the Green dyadics and sources are random quantities, i.e.,

$$[\underline{x}] = \left[\underline{\underline{G}}\right]\cdot[\underline{P}]\,. \tag{4}$$

For a particular constellation of sources, $[\underline{\underline{g}}]$ fixes $[\underline{P}]$ as $[\underline{p}] = [\underline{\underline{g}}]^{-1}\cdot[\underline{x}] \triangleq [\underline{\underline{h}}]\cdot[\underline{x}]$. Here, $[\underline{\underline{h}}]$ is the separation matrix, which is akin to the loading matrix $\underline{\underline{a}}$ in PCA, both being transformation matrices operating on the measured data to yield independent or uncorrelated components from linear combinations of the data, respectively. Although $[\underline{\underline{g}}]$ is indeterminate without prior information on sources, a matching set of estimates for $[\underline{\underline{g}}]$ and $[\underline{p}]$ can be determined together, as shown next.

### D. Complex ICA for UWB Emissions

While standard real-valued ICA ignores phase effects caused by propagation and/or switching delays, several extensions to complex ICA have been proposed for handling complex-valued fields, mixing constants and sources. These deconvolution methods impose different additional restrictions on the individual and global characteristics of the sources; cf., e.g., [19, Table 1], which are not always easy to justify or verify. For example, UWB operation may partially or fully eliminate phase information for individual sources to different degrees or impose different degrees of circularity on different sources. This hampers the identification of unique prior source characteristics.

For narrowband analytic fields, their real and imaginary parts correspond to in-phase and quadrature components at individual frequencies, respectively. For incoherent fields, e.g., UWB fields, propagating/dissipating and reactive power in the evanescent NF can be associated with the real and imaginary parts of the complex-valued power flux, respectively. The reactive power represents the imbalance between time-averaged electric and magnetic power. For the sources, a similar division for its complex emitted power can be made into contributions by propagating and evanescent emitted powers. The source excitations, Green dyadics and measured data then relate to powers/energies instead of fields. Nevertheless, the ICA procedure for either complex powers/energies is mathematically completely analogous to that for complex fields.

## III. Complex ICA Using Maximum-Likelihood Estimation (MLE) with Natural Gradient

### A. Iterative Method

Several approaches exist for the ICA extraction of the quasi-independent sources from their observed mixed field states [20]. The majority of these methods assume and maximize non-Gaussianity of the source probability density functions (PDFs) as a baseline criterion for separation, while generally also implicitly assuming that the PDFs are symmetric as a simplifying assumption. MLE [21], [22] is an accurate, robust and efficient estimation technique that is more versatile because it also applies to skewed PDFs for the sources, in particular, to source *energies*.

Typically, one starts by centering, standardizing, and decorrelating the measured field data $\underline{X}$ to $\underline{Z} \triangleq (\underline{X} - \overline{\underline{X}})/s_{\underline{X}}$ such that $\overline{\underline{Z}\,\underline{Z}^{\dagger}} = \underline{\underline{I}}$, where $\overline{X}$ and $s_{\underline{X}}$ are the sample average and standard deviation across all observations, respectively. This can be done by PCA preprocessing. The real and imaginary parts of the standardized complex intensity $\underline{Z} = \underline{Z}' + \mathrm{j}\underline{Z}''$ represent the standardized sample intensities (or energies) $\underline{Z}'^{(\prime)} \triangleq (|\underline{X}'^{(\prime)}|^2 - \overline{|\underline{X}'^{(\prime)}|^2})/s_{|\underline{X}'^{(\prime)}|^2}$ for the separated propagating field $\underline{X}' = \mathrm{Re}(\underline{X}') + \mathrm{jIm}(\underline{X}')$ and reactive evanescent field $\underline{X}'' = \mathrm{Re}(\underline{X}'') + \mathrm{jIm}(\underline{X}'')$.

[4] For scatterers, the expansion involves spatial derivatives $\underline{\nabla}\,\underline{\nabla}\ldots\underline{\nabla}\underline{\varphi}$ of a source field $\underline{\varphi}$ [16].

[5] Strictly, ICA can extract only as many ICs as the number of observations, $M$, hence $N \leq M$, ideally $N = M$. For $N > M$, source separation is possible only under certain conditions (e.g., spectrally nonoverlapping sources).

If $\underline{\underline{g}}$ were known while $\underline{Z}$ is random, then variate transformation for a vector of $N$ independent sources, arrayed as $\underline{P} = \underline{\underline{g}}^{-1} \cdot \underline{Z}$, would yield the conditional PDF of $\underline{Z}$ as

$$f_{\underline{Z}|\underline{\underline{H}}}(\underline{z}|\underline{\underline{h}}) = |\det(\underline{\underline{h}})| f_{\underline{P}}(\underline{p}) = |\det(\underline{\underline{h}})| \prod_{n=1}^{N} f_{P_n}(p_n = \underline{h}_n^T \cdot \underline{z}) \tag{5}$$

where the source separation (transfer) matrix $\underline{\underline{h}} = \underline{\underline{g}}^{-1} = [\underline{h}_1 \underline{h}_2 \dots \underline{h}_N]^T$ with rows $\underline{h}_n^T$ is assumed to exist (square nonsingular $\underline{\underline{g}}$). The likelihood of the measured field data is the product of their PDFs based on $M$ observations, i.e.,

$$L(\underline{\underline{h}}) \triangleq f_{\underline{Z}_1,\dots,\underline{Z}_M}(\underline{z}_1,\dots,\underline{z}_M|\underline{\underline{h}}) = \prod_{m=1}^{M} f_{\underline{Z}_m}(\underline{z}_m|\underline{\underline{h}})$$

$$= |\det(\underline{\underline{h}})|^M \prod_{m=1}^{M}\prod_{n=1}^{N} f_{P_n}(\underline{h}_n^T \cdot \underline{z}_m). \tag{6}$$

Denoting averaging over the $M$ observations with an overbar, the sample mean likelihood is, thus,

$$\overline{\ln[L(\underline{\underline{h}})]} = \overline{\sum_{n=1}^{N} \ln[f_{P_n}(\underline{h}_n^T \cdot \underline{z}_m)]} + \ln|\det(\underline{\underline{h}})|. \tag{7}$$

Maximization of $\overline{\ln[L(\underline{\underline{h}})]}$ is obtained by selecting its matrix negative gradient in the complex parameter space for $\underline{\underline{h}}$, i.e., differentiation with respect to $\underline{\underline{h}}^*$. The conjugate differentiation of the composite complex function (7) is detailed in the Appendix. In the limit $M \to +\infty$, this gradient follows from (25) as

$$\frac{\partial\langle\ln[L(\underline{\underline{h}})]\rangle}{\partial \underline{\underline{h}}^*} = \langle \underline{\phi}(\underline{\underline{h}} \cdot \underline{Z})\underline{Z}^\dagger\rangle + (\underline{\underline{h}}^\dagger)^{-1} \tag{8}$$

where $\langle\cdot\rangle$ denotes ensemble averaging with respect to $m$, and where the vector of complex *score functions* $\phi_n$ for the sources $P_n = \underline{h}_n^T \cdot \underline{Z} \triangleq P_n' + \mathrm{j}P_n''$ is given by (26)–(27), i.e.,

$$\underline{\phi} \equiv [\phi_n(\hat{p}_n)] \triangleq \left[2\frac{\partial[f_{P_n,P_n^*}(\hat{p}_n,\hat{p}_n^*)]/\partial\hat{p}_n^*}{f_{P_n,P_n^*}(\hat{p}_n,\hat{p}_n^*)}\right]_{n=1}^{N} \tag{9}$$

$$= \left[\frac{1}{f_{P_n',P_n''}(\hat{p}_n',\hat{p}_n'')} \times \left(\frac{\partial f_{P_n',P_n''}(\hat{p}_n',\hat{p}_n'')}{\partial \hat{p}_n'} + \mathrm{j}\frac{\partial f_{P_n',P_n''}(\hat{p}_n',\hat{p}_n'')}{\partial \hat{p}_n''}\right)\right]_{n=1}^{N} \tag{10}$$

in which $P_n$ is estimated from the measured field vector $\underline{z}_m^T$ as $\hat{p}_n = \underline{h}_n^T \cdot \underline{z}_m$. In order for the ascent in (8) at an up-to-date location estimate $\underline{\underline{h}}_i$ to be steepest also in non-Euclidean parameter spaces, the *natural* gradient should be used. This is obtained by postmultiplying (8) with $\underline{\underline{h}}^\dagger \cdot \underline{\underline{h}}$ [23]–[25]. At iteration $i+1$, the separation matrix is $\underline{\underline{h}}_{i+1} = \underline{\underline{h}}_i + \Delta\underline{\underline{h}}_i$, where

$$\Delta\underline{\underline{h}}_i = \frac{\partial\langle\ln[L(\underline{\underline{h}}_i)]\rangle}{\partial \underline{\underline{h}}_i^*} \cdot \left(\underline{\underline{h}}_i^\dagger \cdot \underline{\underline{h}}_i\right)$$

$$= \left(\underline{\underline{I}} + \langle \underline{\phi}(\underline{\underline{h}}_i \cdot \underline{Z})(\underline{\underline{h}}_i \cdot \underline{Z})^\dagger\rangle\right) \cdot \underline{\underline{h}}_i. \tag{11}$$

The estimate $\hat{\underline{\underline{h}}}$ is reached asymptotically when all (non)linear correlations have vanished, i.e., $\langle \underline{\phi}(\underline{\underline{h}}_i \cdot \underline{Z})(\underline{\underline{h}}_i \cdot \underline{Z})^\dagger\rangle \to -\underline{\underline{I}}$.

In summary, when perturbing an arbitrary initial estimate of the separation matrix $\underline{\underline{h}}_0$ by an amount $\alpha_0 \Delta\underline{\underline{h}}_0$ according to

$$\underline{\underline{h}}_{i+1} = \underline{\underline{h}}_i + \alpha_i \Delta\underline{\underline{h}}_i = \left(2\underline{\underline{I}} + \alpha_i \overline{\underline{\phi}(\underline{\underline{h}}_i \cdot \underline{z}_m)(\underline{\underline{h}}_i \cdot \underline{z}_m)^\dagger}\right) \cdot \underline{\underline{h}}_i \tag{12}$$

this generates an iterative process of successive approximations $\{\underline{\underline{h}}_i\}_{i=1}^{\infty}$ that yields improved estimates for $\underline{\underline{h}}$ and for the ICs $\underline{p}$ as $\hat{\underline{p}}_i = \underline{\underline{h}}_i \cdot \underline{z}_m$. In (12), the adaptive constant $\alpha_i$ where $|\alpha_i| < 1$ can be adjusted between iterations to maximize the rate of convergence while maintaining numerical stability. In practice, the iterative process can be terminated when the relative step change $\varepsilon_i = \|\Delta\underline{\underline{h}}_i\|/\|\underline{\underline{h}}_i\|$ falls below a specified threshold $\varepsilon_{\max}$. For large $M$, the sample averaging in (12) at each iteration step can be circumvented by replacing it with the currently observed value of the overlined expression, thus using a *stochastic* natural gradient rule for updating.

The final estimate $\hat{\underline{\underline{h}}}$ and the extracted estimated ICs $\hat{\underline{p}} = \hat{\underline{\underline{h}}} \cdot \underline{z}$ yield the MLE of the mixing matrix $\underline{\underline{g}}$, by (pseudo) inversion or by maximum *a posteriori* probability (MAP) estimation, in case of an overcomplete basis (cf., Section III-C), as

$$\hat{\underline{\underline{g}}} = (\underline{z}_m \underline{z}_m^\dagger) \cdot (\underline{z}_m \hat{\underline{p}}^\dagger). \tag{13}$$

### B. MLE Score Functions for UWB Energy Sources

For incoherent sources, one wishes to apply ICA also to *skewed* PDFs $f_{P_n}(p_n)$, as is typical for the intensity, energy, power, and other square-law or more general nonlinear functions $P_n$. For practical reasons explained in Section IV-A, it is further assumed that $P_n$ and hence $\phi_n$ are real valued, leading to a 1-D $f_{P_n}(p_n)$ per source. For ideal[6] random EM fields produced by a set of $s_n$-dimensional incoherent circular source currents, such $P_n$ exhibit a $\chi^2_{2s_n}$ PDF [7]: after standardization of $P_n$ to $Z_{P_n}$,

$$f_{Z_{P_n}}(z_{P_n}) = \frac{s_n^{s_n/2}}{\Gamma(s_n)}\left(z_{P_n} + \frac{\langle P_n\rangle}{\sigma_{P_n}}\right)^{s_n-1} \times \exp\left(-\sqrt{s_n}\left(z_{P_n} + \frac{\langle P_n\rangle}{\sigma_{P_n}}\right)\right) \tag{14}$$

for $p_n \geq 0$, i.e., $z_{P_n} \geq -\langle P_n\rangle$ and zero otherwise (active nonabsorbing radiating sources). For realistic sources, $s_n$ is variable and may serve as a distribution parameter (gamma PDF). Because of the previously mentioned ambiguity in ICA, we may fix the expected value and use instead the simpler form

$$f_{P_n}(p_n) = \frac{s_n^{s_n/2}}{\Gamma(s_n)} p_n^{s_n-1} \exp(-\sqrt{s_n}p_n). \tag{15}$$

[6]The distributions (14) assume that the number of degrees of freedom per source is exceedingly large, so that each $\underline{j}_n$ exhibits an approximately Gaussian latent prior PDF, on account of the central limit theorem. For relatively low numbers of degrees of freedom, a Bessel $K$ or more general sampling PDF for the energy is appropriate [26].

Applying (28) to (15) results in the hyperbolic score function

$$\phi_n(p_n) = \frac{s_n - 1}{p_n} - \sqrt{s_n}. \tag{16}$$

The case $s_n = 1$ yields a constant $\phi_n$, which cannot be used in the gradient search. However, $s_n = 1$ corresponds to a negative exponential distribution associated with circular Gaussian sources, which is excluded from ICA anyway. Physically, this represents a unidirectional random source current that is a circularly symmetric (e.g., electric dipole antenna with unmodulated random current). On the other hand, for $s_n \neq 1$, (16) becomes unbounded for $p_n \to 0$. To avoid instabilities during the gradient search, the pole of $\phi_n(p_n)$ can be shifted away from the real axis into the complex $p_n$-plane, by defining

$$\phi_n^{(0)}(p_n) \triangleq (s_n - 1)\mathrm{Re}\left(\frac{1}{p_n + \mathrm{j}\theta_n}\right) - \sqrt{s_n} \tag{17}$$

Thus, the free parameter $\theta_n$ creates a "damping" of the "resonance" for $\phi_n(p_n)$, shifting its maximum from $p_n = 0$ to $\theta_n$. Since all $\chi^2_{2s_n}$ PDFs for $s_n > 1$ start at the origin, this $\phi_n^{(0)}(p_n)$ is a feasible parametric approximation.

MLE can be iterated semiparametrically by devising an appropriate pair of approximating but discriminating score functions $\phi_n^{(\pm)}(p_n)$ [11]. In the ICA for *fields*, the chosen forms of $\phi_n^{(\pm)}(p_n)$ are governed by the adopted metric of non-Gaussianity and the latent PDFs $f_{P_n}(p_n)$ are assumed to be even (symmetric) but otherwise unknown. For such zero skewness, only an odd (antisymmetric) nonlinear score function is needed to achieve independence, e.g., using the inverted sigmoid $\phi_n^{(s)}(p_n) = 1 - 2/(1 + \exp(-p_n))$. However, this only forces the *even* nonlinear and *pairwise* correlations to be eliminated (via the nonlinear covariance term $\underline{\phi}(\underline{\hat{p}}_i)\underline{\hat{p}}_i^{\dagger}$ in (12) with $\underline{\phi} = \underline{\phi}^{(s)}$), leaving remainder residual correlations if $f_{P_n}(p_n)$ is skewed. Thus, in order for $\phi_n$ to include also contributions by all even powers of $p_n$ when the source PDF is skewed, an appropriate nonlinear *even* function must be added, e.g.,[7]

$$\phi_n^{(\pm)}(p_n) \triangleq \phi^{(0)}(|p_n|) \mp \left(\frac{2}{1 + \exp(-p_n)} - 1\right) + a^{(\pm)} \tag{18}$$

for thin or heavy tailed $f_{P_n}(p_n)$, respectively. These $\phi_n^{(\pm)}(p_n)$ remain bounded for any value of $p_n$. Their associated contrast (i.e., cost) functions $\Phi_n^{(\pm)}(p_n)$ are as follows:

$$\Phi_n^{(\pm)}(p_n) \triangleq \int \phi_n^{(\pm)}(p_n)\mathrm{d}p_n = (a^{(\pm)} - \sqrt{s_n})p_n + \frac{s_n - 1}{2}\ln(p_n^2 + \theta_n^2) \mp 2\ln\left(\cosh\frac{p_n}{2}\right). \tag{19}$$

The constants $a^{(\pm)}$ in (18) and (19) can now be omitted *a posteriori* because $f_{P_n}(p_n) = \exp(\Phi_n^{(\pm)}(p_n))$ are positive functions regardless, as required for representing PDFs. The choice between $\phi_n^{(+)}$ and $\phi_n^{(-)}$ per iteration can be decided based on the skewness or excess kurtosis of $\exp(\Phi_n^{(\pm)})$. Fig. 2 shows (17), (18), and (19) for $s_n = 2$ at selected values of $\theta_n$. The thin and

[7]Note that invertibility of $\phi_n^{(\pm)}(\cdot)$ is not strictly required.

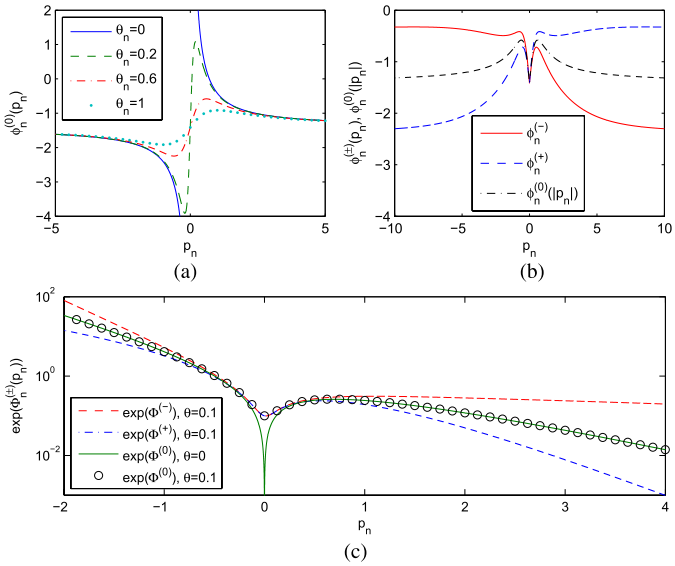


Fig. 2. (a) Stabilizing score function $\phi_n^{(0)}(p_n)$ for $s_n = 2$ and selected values of $\theta_n$. (b) Bifurcated score functions $\phi_n^{(\pm)}(p_n)$ for iterative gradient searching with $s_n = 2$ and $\theta_n = 0.6$. (c) Associated source PDFs $\exp(\Phi_n^{(\pm)}(p_n))$ for $s_n = 2$ and $\theta_n = 0.1$, compared with $\Phi_n^{(0)}(p_n) \equiv \int \phi_n^{(0)}(p_n)dp_n$ for $\theta_n = 0.1$ and $\theta_n = 0$. For active nonabsorbing sources, $p_n \geq 0$.

heavy tail characteristics of $\exp(\Phi_n^{(+)}(p_n))$ and $\exp(\Phi_n^{(-)}(p_n))$, respectively, are clearly witnessed.

Thus, pairwise statistical independence defined by

$$\langle (P_{n_1})^{k_1} \ldots (P_{n_\nu})^{k_\nu} \rangle = \langle (P_{n_1})^{k_1} \rangle \ldots \langle (P_{n_\nu})^{k_\nu} \rangle \tag{20}$$

with $\nu = 2$, for any even value of $k_1 + k_2$ and arbitrary source pair $(n_1, n_2)$, can be approached arbitrarily closely by using (18). For non-Gaussian $f_{P_n}(p_n)$, any residual *multivariate* correlations between $\nu$-tuples of sources ($\nu > 2$) must also vanish for full statistical independence, but remain unaccountable. For frequency-domain deconvolution, $P_n$ is complex even when the data $\underline{\underline{z}}$ are real. In this case, an appropriate complex score function is $\phi_n^{(\pm)}(p'_n) + \mathrm{j}\phi_n^{(\pm)}(p''_n)$.

### C. UWB Source Estimation for Overcomplete Bases

When $M = N$, the ICs can be uniquely identified, up to a scale factor and neglecting source hierarchy [9]. When $M > N$, it becomes possible to account for noise in the observations.[8] Here, with the exception of Section IV-B3, we focus instead on the case where there are far fewer field observations ($M \ll N$), as is typical for NF measurements on ULSI circuits. Such so-called overcomplete representations [27] (underdetermined systems) are more difficult to characterize if the prior PDF is skewed, as in (15). For $M < N$, the ICA source model applies to an $M$-dimensional subspace spanned by sampled observations, which lies in the $N$-dimensional signal space spanned by all emission sources and which can be chosen in

[8]In complex ICA with maximum one circular Gaussian source (cf. footnote 3) and $M = N$, only background noise can be separated from the signals as a single "source."

$N!/[M!(N-M)!]$ different ways. Hence, the expansion in independent sources is not unique, but can be optimized by MAP estimation. Nevertheless, we shall find from experimental results that ICA is still capable of producing restricted EM source decompositions that yield reasonably accurate emission maps (up to an aforementioned scale factor), even for large compression ratios $M/N$. Of course, it is always possible to limit a full area of scanned points into $N/N'$ subregions, each containing $N'$ points, and then determine $N' = M < N$ ICs per subregion at a time. However, in this case, the source patterns become fragmented because of the scaling ambiguity.

## IV. Experimental Results

### A. Design of Experiments

Observations were generated at up to 401 evenly spaced frequencies, by collecting NF data with a scanning magnetic field probe. This number is a factor 3 or more smaller than the number of spatial scan (grid) points. Each grid point constitutes a variable in the search for ICs that are linear combinations of these variables. The number of scan points is the maximum number of potential spatial ICs. The use of the single-axis field probe does not allow for the local Poynting vector to be determined and, hence, for the reactive energy of the evanescent NF to be separated from the propagating (far-field) energy. Therefore, we only perform ICA on the real-valued intensity of the tangential magnetic field $|H_t|^2$, i.e., on the squared magnitude of the raw combined fields ($\underline{Z} = \underline{Z}'$). Alternatively, complex ICA on the I/Q fields could have been performed. ICA iterations were performed using the score functions (18) with $\theta_n = 0.1$ and were terminated when reaching an approximation error less than $\varepsilon_{\max} = 10^{-5}$. For the extracted complex ICs, only results for their amplitudes are shown because of space limitations.

MLE with adaptive nonlinearity (where the adaptation is decided by the sign of the skewness or excess kurtosis) is known to produce smallest statistical errors, particularly for large $N$, and was therefore implemented despite its slower convergence [28]. Except for the determination of individual ICs in Section IV-B1, a natural gradient algorithm based on batched data was preferred over sampled stochastic gradients because of lower sensitivity to the data particulars and faster convergence.

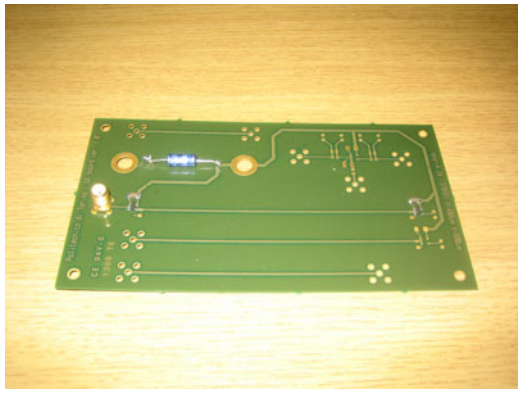

Fig. 3. Microstrip transmission line inverter circuit.

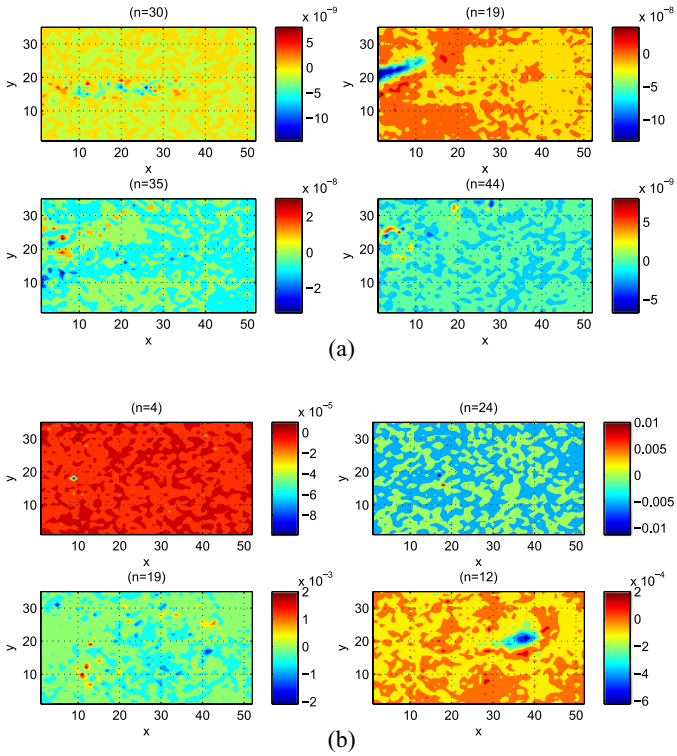


Fig. 4. Selected representative ICs, based on (a) $M = 51$ ($N = 50$) and (b) $M = 401$ ($N = 400$) observation frequencies.

### B. Analog Circuit: Transmission-Line-Based Inverter

We measured a microstrip transmission line circuit with added lumped circuit elements (capacitor, inverters) and vias (see Fig. 3). The circuit was scanned in a parallel horizontal plane at 10-mm height, across a uniform grid of $P = 52 \times 35 = 1820$ points with spacing of 5 mm in $x$- and $y$-direction. $H_x$ and $H_y$ were measured from 600 to 3000 MHz in increments of 6 MHz.

*1) IC Maps, Amplitude Matrix, and Reconstructed Emission Patterns:* Fig. 4(a) shows location maps for four typical randomly selected ICs, based on $M = 51$ observation frequencies across 600–900 MHz. Because of the relatively large compression ($M/P \simeq 1/35$), ICs incorporate a significant part of the spatial patterns and geometrical features at individual frequencies. Most IC maps contain spatially scattered or conglomerated peaks, while very few single-peak maps (sparse ICs) arise. This field structure is in marked contrast with ICs for natural images, which typically consist of edge patterns [11].

Increasing the number of observations to $M = 401$ frequencies ($M/P \simeq 1/4.5$) across 600–3000 MHz results in IC maps typical of those shown in Fig. 4(b). Most IC maps now exhibit a single positive or negative large peak (e.g., for $n = 4$), while some exhibit a pair (for $n = 24$) or even a set (for $n = 19$) of isolated peaks of equal or opposite polarity. Exceptionally, the peaks may still form an extended cluster (for $n = 12$). Recall that the maximum amplitudes of the raw extracted ICs are irrelevant in ICA.

Spiky IC maps, such as those in Fig. 4(b) for $n = 4$, have been ascribed [29] to the case where the number of extracted

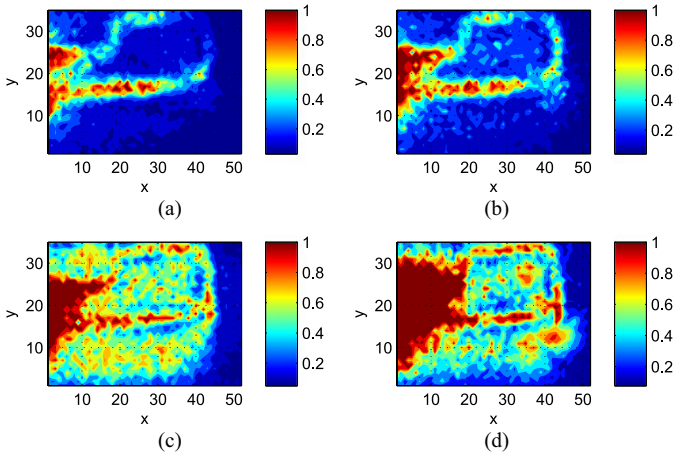


Fig. 5. Summary plots of all $N$ extracted ICs, after equalization per observation frequency: (a) $N = 50$ (600–900 MHz; $M = 51$), (b) $N = 100$ (600–1200 MHz; $M = 101$), (c) $N = 200$ (600–1800 MHz; $M = 201$), (d) $N = 400$ (600–3000 MHz; $M = 401$).

ICs is much larger than required for adequately explaining and modeling the actual measured spatial field pattern $z_m$, i.e., an overspecification of the statistical model. Thus, *a posteriori*, an adequate ICA model could have been obtained with a considerably coarser grid. Spikes are also indicative of strong frequency dispersion between spatial maps (nonidentically distributed ICs with regard to observation frequency). To avoid overspecification, one can select fewer observations ($M' \sim N \ll M$), e.g., by applying Cattell's rule, provided there is a sufficiently large SNR between the emission sources and measurement noise, with distinct eigenvalues.

Fig. 5(a) shows an overlay of all 50 IC maps, indicating spatial locations that feature in any of the maps for individual frequencies in the 600–900-MHz band ($M = 51$). This enables all extracted ICs to be combined into a single plot. The map was obtained after normalization of each $n$th IC map by its maximum modulus value reached at some (IC dependent) location $(x_n, y_n)$. Even for this relatively low value of $M$, where the model is underspecified, the lining of current sources along the actual conduction path is clearly discernable, which is not apparent from individual IC maps. As $M$ and hence $N$ increase, more source points become visible[9] [see Fig. 5(b)–(d)], ultimately lining the entire current loop and the vicinity of the coaxial connector, where most of the emissions arise. At the same time, the increased noise as a result of overspecification becomes apparent.

Typical convergence profiles for the iterative IC calculation are shown in Fig. 6. Occasionally, the instantaneous error dwells around a local minimum before decreasing below $\varepsilon_{\max}$, here chosen as $10^{-5}$. As can be seen, smaller values of $M$ do not guarantee faster convergence.

Regarding the reconstruction of emission patterns, the extracted ICs form basis functions. Their corresponding amplitudes at each frequency are the rows of $[\underline{\underline{h}}]$. These are shown

[9]Since many ICs have multiple peaks, the total number of peaks in the summary plot is larger than $M$.

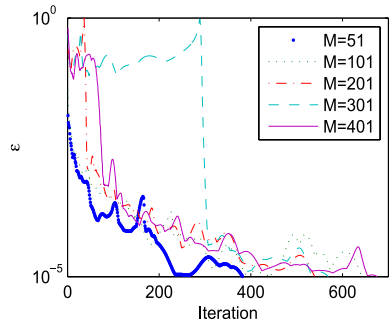


Fig. 6. Typical sample paths for relative magnitude of perturbation of synthesis matrix $\varepsilon_i = \|\Delta \underline{\underline{h}}_i\| / \|\underline{\underline{h}}_i\|$ iterations in ICA for full scan ($52 \times 35$ locations), converging to within $\varepsilon_i \leq \varepsilon_{\max} \stackrel{\Delta}{=} 10^{-5}$, for selected number of observation frequencies $M$.

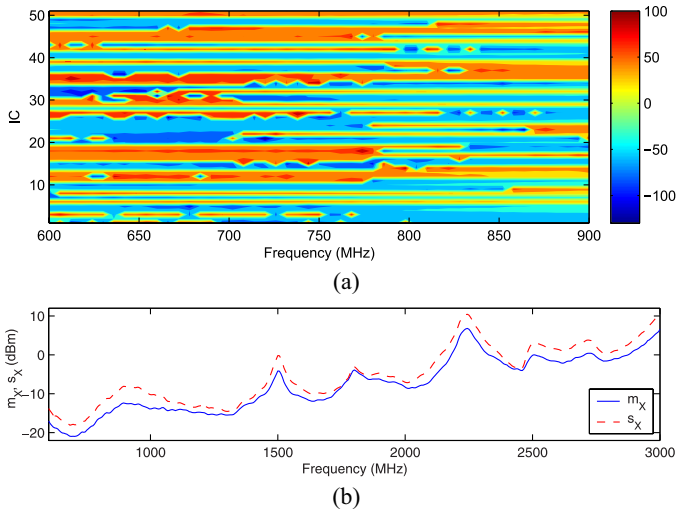


Fig. 7. (a) Extracted IC amplitudes (in signed dB) as a function of frequency for $N = 50$, $M = 51$ (600–900 MHz). (b) Spatial mean and standard deviation (dBm) of measured tangential field intensity $|H_t|^2$ across full frequency band.

on a signed decibel scale in Fig. 7(a). Generally, larger fluctuations with IC numbers are seen at lower frequencies. Differences between amplitudes remain fairly constant over relatively large frequency intervals, as indicated by the striped pattern. Fig. 7(b) shows that the ratio of the standard deviation to the mean for the energy fluctuates between 0 and 4.5 dB across frequency. This is substantially larger than the theoretical value $10 \log_{10}(\sqrt{2}/2) = -1.51$ dB for the $\chi^2_4$ distribution of an ideal random $|H_t|^2$ (i.e., (15) with $s_n = 2$).

For the reconstructed emission maps based on the extracted ICs, their magnitudes[10] for $N = 50$ are shown in Fig. 8(a) for four selected frequencies below 900 MHz. Despite being composed on the basis of just 50 ICs for 1820 scan locations, the main features of the field at each frequency are reconstructed well by the ICA [compare with Fig. 8(c)]. When using 401 observations spanning 600–3000 MHz, [see Fig. 8(b)], the accuracy at the selected frequencies improves further, as expected.

[10]Note that the value of an IC coefficient at a given location need not be positive; only $\sum_{n=1}^{N} \underline{g}_{mn} \cdot \underline{p}_n$ involving all ICs for that location should equal the intensity of the measured field, $|\underline{H}_t|^2 > 0$.

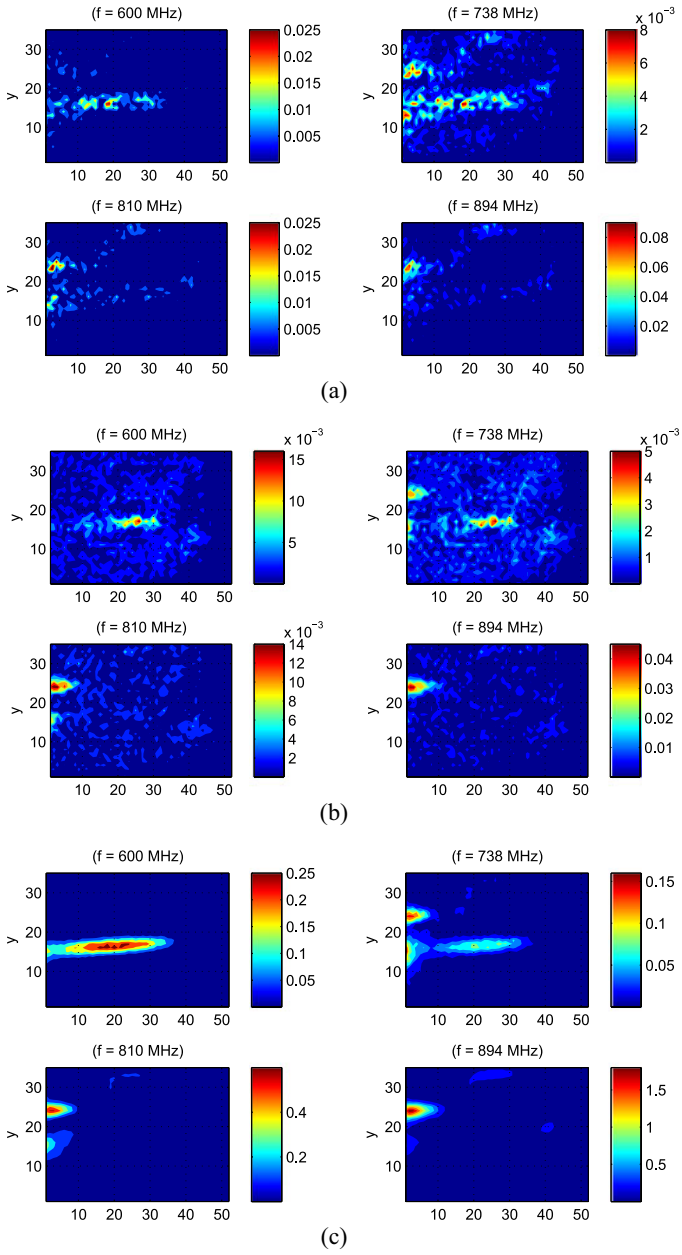


Fig. 8. IC-based reconstructed spatial maps of emissions for $|H_t|^2$ at selected frequencies below 900 MHz, based on extracted ICs for (a) $M = 51$, $N = 50$ (600–900 MHz), (b) $M = 401$, $N = 400$ (600–3000 MHz), (c) reference measured values.

Interestingly, this is achieved through additional observations at frequencies *different* from the selected ones, i.e., by including the data for 906–3000 MHz.

To examine the influence of the number of extracted ICs on the ICA calculations, we compared results for $M = 51$, 101, 201, 301, and 401 observation frequencies. For the full scanned area ($P = 1820$), this leads to $N = M - 1$ extracted ICs. Batch processing, i.e., computing each IC by using the complete set of data points from the start of the scan, is preferred over incremental updating, where the ICs are adjusted after each new scanned location. The former leads to greater numerical stability in the gradient search and a lower number of iterations for

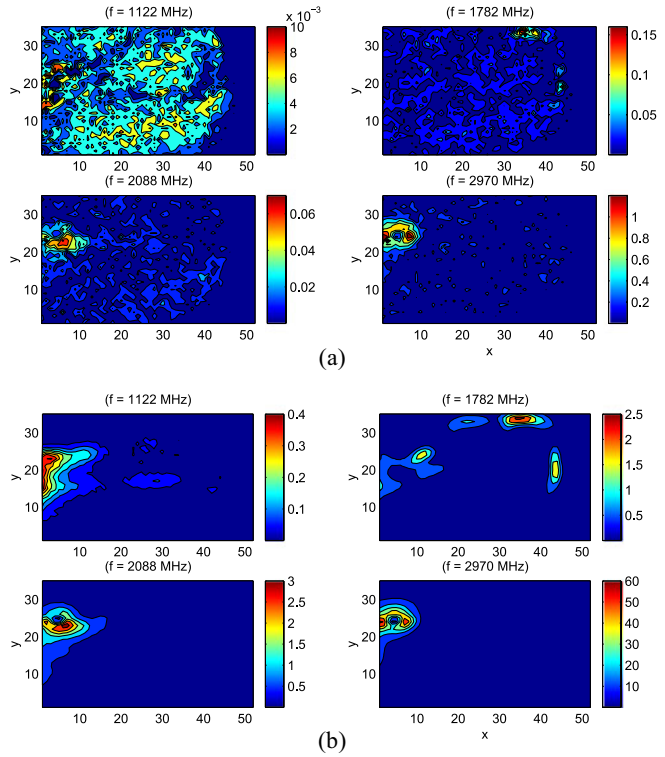


Fig. 9. Spatial distribution of $|H_t|^2$ at selected frequencies between 600 and 3000 MHz: (a) ICA based on 400 extracted ICs, (b) measured.

convergence, at the expense of a somewhat increased time per iteration step. Convergence to within $\varepsilon_{\max}$ was achieved after 139, 205, 266, 277, and 285 iterations, taking 2.04, 6.53, 26.10, 38.4, and 57.6 s to complete on a state-of-the-art desktop PC, respectively, when starting from a random matrix $\underline{\underline{h}}_0$. These computational costs are obtained for relatively low numbers of iterations and come with the higher numerical stability that is typical of batch processing, compared to the purely stochastic method of incremental updating that is faster per iteration but requires considerably more cycles to convergence. Thus, batch processing is feasible for ICA of circuit fields.

*2) Estimated Emissions Maps at Higher Frequencies:* Reconstructions of emissions at selected frequencies between 900 and 3000 MHz based on extracted ICs are shown in Fig. 9 for $M = 401$ ($N = 400$). When the dynamic range of the measured $|H_t|^2$ is relatively small (e.g., at 1122 MHz), a reconstruction based on a still relatively small number of observations ($M/P = 401/1820 = 22\%$) becomes more difficult: several zones with spurious sources now appear in Fig. 9(a) compared to Fig. 9(b) because these ICs do not superimpose to zero at these locations, as would have been the case if all ICs had been extracted. As the measured field becomes more spatially concentrated and acquires a larger dynamic range, the reconstruction quality improves (e.g., at 2970 MHz).

Superimposing all spatial maps of extracted ICs [see Fig. 10(a)] and comparing the result with the superimposed measured emissions across all frequencies [see Fig. 10(b)] gives, in a single plot, an indication of the accuracy of the ICA result across the entire band. Thus, the main wideband emissions are

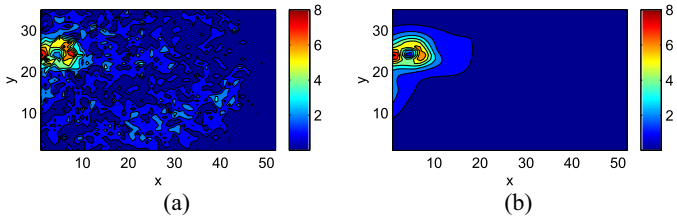


Fig. 10. Spatial distribution of total wideband $|H_t|^2$ across 600 to 3000 MHz: (a) ICA with 400 ICs, (b) measured.

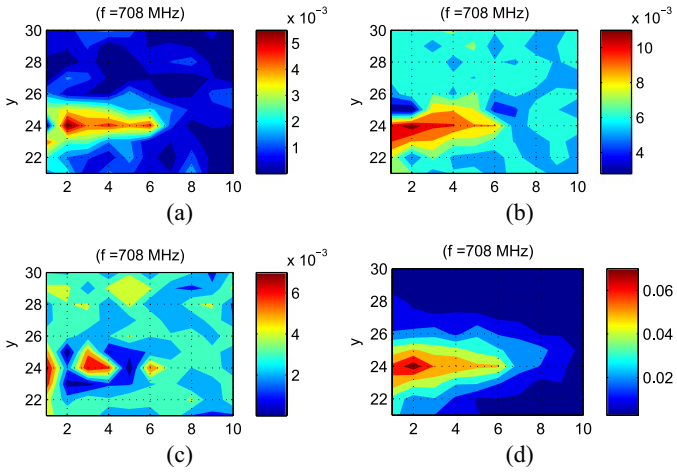


Fig. 11. IC-based reconstructed spatial maps of $|H_t|^2$ at 708 MHz for scanned subregion $(1-10)\times(21-30)$, based on $N$ extracted ICs: (a) 600–900 MHz ($M=51$), $N=51$; (b) 600–1200 MHz ($M=101$), $N=95$; (c) 600–3000 MHz ($M=401$), $N=99$; (d) reference measured values.

seen to be around the connector and are well predicted from 401 observations. Since HF contributions dominate in this summary plot, one could have chosen far fewer ICs but at the higher frequencies. This would suffice to get an IC representation of comparable accuracy.

*3) Overcomplete versus Undercomplete Bases:* In the previous analysis, the IC basis is strongly overcomplete ($M \ll P$). To compare the quality of this estimation with complete ($M=P$) and undercomplete ($M>P$) bases, we focus on a subarea of scan size $P=100$ points $(1\le x\le 10, 21\le x\le 30)$, using the same set of frequencies as before. By way of example, emissions at 708 MHz are evaluated, where the scanned subarea represents a radiation hot spot. The results in Fig. 11 show that, remarkably, the reconstruction quality now *decreases* with increasing $M$. This can be understood by noting that, given a sufficiently large value of $M$ and hence $N$, the ICA algorithm preferentially chooses those ICs that include locations where most of the spatial detail occurs, i.e., involving disproportionally more ICs at higher frequencies. Consequently, for, e.g., $M=401$ across 600–3000 MHz, one expects less than the proportional 50 ICs to be assigned to those spatial patterns that constitute the maps for the 600–900-MHz band, whereas for $M=51$ across 600–900 MHz, all ICs are necessarily used.

Oversampling ($N<M$) affects the rate of ICA convergence. Table I compares the numbers of extracted ICs $N$ and the average rate $I$ for convergence to within $\varepsilon_{\max}=10^{-5}$ (averaged over 20 realizations) at selected $M$, for the $10\times 10$ scanned locations. Note that $I=54.9$ at $M=401$ for the $10\times 10$ subarea compared to the sample value $I\sim 500$ at the same $M$ and $\varepsilon_{\max}$ for the full $52\times 35$, demonstrating the effect of over- and undersampling on the ICA convergence.

TABLE 1
AVERAGE NUMBER OF ITERATIONS $I$ FOR CONVERGENCE OF $N$ ICS TO WITHIN $\varepsilon_{\max}=10^{-5}$ AT SELECTED $M$, FOR $P=N_{\max}=100$

| $M$ | 51 | 76 | 101 | 201 | 301 | 401 |
|---|---|---|---|---|---|---|
| $N$ | 51 | 76 | 95 | 99 | 99 | 99 |
| $I$ | 90.6 | 75.0 | 57.9 | 56.6 | 50.3 | 54.9 |

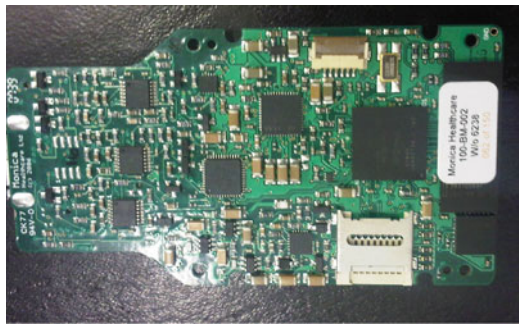

Fig. 12. PCB of health monitoring device based on Bluetooth wireless communication protocol (front view).

## C. Digital Circuit: Bluetooth Transceiver

As a second example, consider emissions from a digital circuit, viz., the transceiver of a portable health monitoring system (see Fig. 12) that uses the Bluetooth communications protocol (2.405–2.480 GHz). This device is battery powered, hence dominant emissions created by a connector as in the previous example are no longer an issue. On the other hand, the device contains an on-board patch antenna at the back of the PCB and a feed wire connecting the battery to the circuit (not shown).

As before, measurements of $H_x$ and $H_y$ were performed and combined to $|H_t|^2=|H_x|^2+|H_y|^2$ by scanning the magnetic field in a horizontal plane at 10 mm above the front of the PCB (components' side) across a uniform grid of spacing 5 mm, now for $P=44\times 28=1232$ locations. The 2.400–2.500-GHz band was sampled at increments of $\Delta f=250$ kHz ($M=401$ observation frequencies), corresponding to half of the spectral spacing between the Bluetooth frequency components. Odd multiples of 250 kHz coincide with visited hop frequencies, while even multiples carry no transmissions and have magnitudes that are tens of decibel lower. Preliminary PCA was performed in order to reduce the sample space, which retained 276 PCs (276/401 = 68.8%) with eigenvalues larger than $10^{-7}$. This warrants the nonsingularity of the covariance matrix. The ICA iterations were again terminated when $\varepsilon<10^{-5}$, which was achieved after typically 145 iterations in 20.5 s.

*1) Spatial IC Maps:* Fig. 13 summarizes all 276 superimposed ICs, after equalization by their respective maximum amplitudes. The influence of the radiating antenna located in the top left corner is verified to be a major contribution.

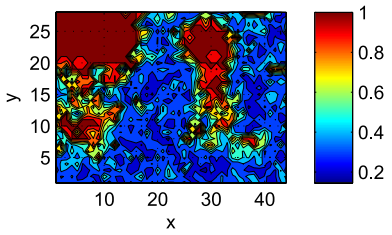


Fig. 13. Summary plot of all 276 extracted ICs across the 2.4–2.5-GHz band, after normalization of each IC by its maximum value.

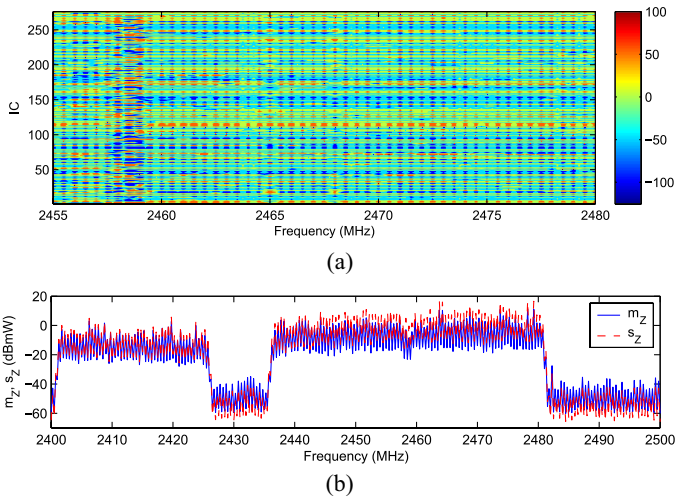


Fig. 14. (a) Frequency distribution of IC amplitudes (in signed decibel) across the upper part of the Bluetooth band for $N = 276$ individual ICs. (b) Spatial mean and standard deviation of the measured $|H_t(f)|^2$.

*2) IC Amplitudes:* The mixing matrix containing the discrete IC amplitudes across a selected subband is shown in Fig. 14(a). Compared to the analog circuit of Section IV-B, the IC amplitudes are now discrete and spectrally more uniform in value with respect to in-band frequencies. For certain frequencies (e.g., 2458–2459 MHz), the amplitudes change their polarity rapidly. For any IC, its in-band amplitudes are relatively constant across frequency, as confirmed by the mean and standard deviation across the scanned plane for the measured signal values, shown in Fig. 14(b).

*3) Measured versus IC-Based Estimated Emission Maps:* Using all 276 extracted ICs and their associated amplitudes as their weights, the reconstructed emission patterns for six selected frequencies are shown in Fig. 15(a), for comparison with the measured values in Fig. 15(b). This shows that in-band emissions at the hop frequencies (e.g., at $f = 2437.25$ and 2457.25 MHz) exhibit good reconstruction quality in those zones where the highest emission levels occur. Some locations with notable spurious sources occur e.g. at $(x = 5, y = 11)$ due to the aforementioned overcompleteness of the IC basis. In-band emission maps at frequencies in between the Bluetooth comb frequencies are also fairly well reconstructed (e.g., at $f = 2411$ MHz and 2447 MHz), although the effect of noise on the degradation of reconstructed amplitudes for the ICs is now more severe, as expected. Emissions for frequencies that are on or near the edge of the pass bands (e.g., at $f = 2400.75$ MHz) or out of band (e.g., at $f = 2435.5$ MHz) are spatially strongly localized in the plane and are reconstructed well, especially considering their relatively low magnitudes. From comparison of the reconstruction quality at a hop frequency having relatively low-average signal power to the quality at a gap frequency, where the average noise power is much higher (e.g., at $f = 2400.75$ MHz versus $f = 2411$ MHz), it appears that the absolute strength (power) of sources is subordinate to their existence as signal sources and to the strength of their interdependence (higher order correlation) when aiming to identify IC sources.

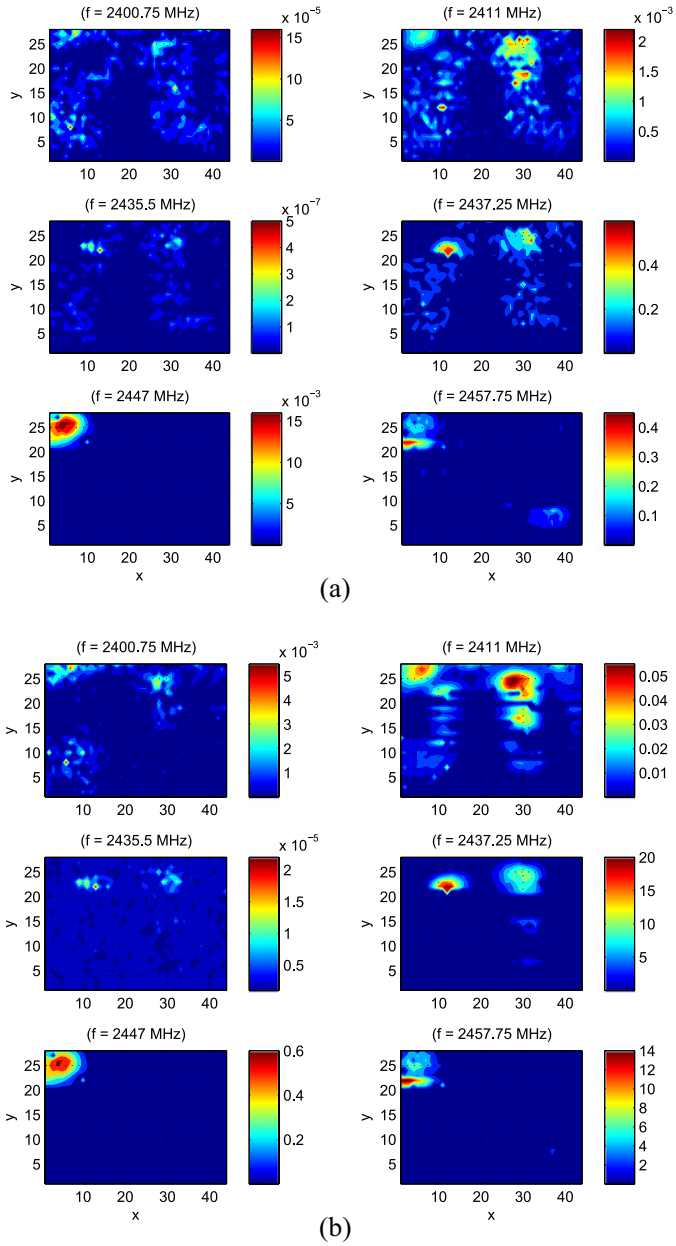


Fig. 15. Spatial distributions of emissions for $|H_t|^2$ at selected frequencies: (a) reconstruction based on $N = 276$ extracted ICs for $M = 401$ observation frequencies; (b) for measured values, based on a scanned grid of $P = 44 \times 28$ locations.

## V. Limitations

When $M = N$, a question arises regarding the relationship between the extracted IC sources and the dipole (or other) physical EM sources corresponding to (3) because ICA does not take retardation effects by wave propagation explicitly into account. For narrowband emissions, ICA is particularly effective in the NF because increasing the distance diminishes the observed correlation[11] between sources (e.g., [30], Fig. 1]). For wideband emissions, however, different frequency components will decay over different heights, hence the measured field at arbitrary height no longer contains information about all source frequencies in the same measure as at source level. In this case, ICA can only separate the surviving (lower frequency) components of the sources. The number of extracted ICs then decreases with increasing height.

In general, the indeterminacy of ICs with regard to their amplitudes does not allow them to be used for estimating IC source values at different measurement locations, unless additional prior information (if only approximate) about the source constellation is available. In the latter case, polynomial chaos (stochastic collocation, spectral methods) may be a more appropriate technique. Furthermore, unlike PCA, where adding more PCs leads to a progressively better model in which the previous PCs are maintained, the ICs obtained from a subset of the data are in general not maintained when $P$ is increased. This is an indirect consequence of the lack of hierarchy and variance explained by the ICs, which makes any already determined ICs not superior to any newly determined one(s). Therefore, ICs are only meaningful as a set, i.e., in a linear combination with each other.

## VI. Conclusion

Several decomposition methods exist for orthogonalization or decorrelation of measured data. Complex ICA allows for maximally independent complex valued sources of EM emission to be extracted. In this paper, this was applied to spatial separation of sources that produce both propagating and evanescent energy in their NF, corresponding to complex (active and reactive) power.

Applied to emissions from circuits, $M$ statistically independent operational conditions (observations) of the circuit follow by parametric variation (here, different frequencies). The number of *independent* realizations that can be realistically generated is often considerably smaller than the number of independent sample values $P$ (here, spatial scan locations) per realization ($M \leq P$), which entails an overcomplete basis for the field. For this scenario, the present results, therefore, demonstrate the feasibility of representing the complete set of emission sources in ULSI circuits with a reduced set of ICs. A unique decomposition into ICs requires $M = P$. This restricts the number of extractable ICs $N$ to be $N \leq M$. Conversely, when the number of samples is more limited than the number of independent observations that can be generated (undercomplete basis), $N \leq P$. For an incomplete basis, $N \leq \min(M, P)$.

Despite this restriction, our analysis of wideband NF emissions shows that hot spots can be accurately represented by a strongly reduced number of statistically independent energy components ($N \ll M$). Depending on the ratio $M/P$, these equivalent sources either correspond to extended physical sources or resemble spatial concentrated regions. Remarkably, using measured emissions patterns at supplementary (higher) frequencies, one achieves better agreement at an intended lower frequency as a result of ICA.

[11] In [30], this was demonstrated for linear correlation and can be understood physically from the fact that the observed intensity at $\underline{r}$ from two sources at $\underline{r}'_1$ and $\underline{r}'_2$ depends on the difference $||\underline{r} - \underline{r}'_1| - |\underline{r} - \underline{r}'_2||$ relative to $||\underline{r} - \underline{r}'_1| + |\underline{r} - \underline{r}'_2||$. This relative difference decreases with increasing average distance, thus increasing the observed linear correlation to a limit. On the same grounds, nonlinear source correlations undergo qualitatively a similar increased correlation with distance.

## Appendix

The chain rule for conjugate complex differentiation [31]

$$\frac{\partial \psi[\varphi(z,z^*)]}{\partial z^*} = \frac{\partial \psi}{\partial z}[\varphi(z,z^*)]\frac{\partial \varphi}{\partial z^*} + \frac{\partial \psi}{\partial z^*}[\varphi(z,z^*)]\frac{\partial \varphi^*}{\partial z^*} \quad (21)$$

can be applied to the first term in (7). With $p_n^* = \underline{z}_m^\dagger \cdot \underline{h}_n$ and noting that $f_{P_n,P_n^*}(p_n, p_n^*) \equiv f^*_{P_n,P_n^*}(p_n, p_n^*)$, this yields

$$\begin{aligned}\frac{\partial \ln[f_{P_n}(p_n)]}{\partial h^*_{nm}} &= \frac{\partial \ln[f_{P_n,P_n^*}(p_n,p_n^*)]}{\partial p_n^*} z^*_{mn} \\ &= \frac{2\, z^*_{mn}}{f_{P_n,P_n^*}(p_n,p_n^*)} \frac{\partial f_{P_n,P_n^*}(p_n,p_n^*)}{\partial p_n^*}. \quad (22)\end{aligned}$$

For the second term in (7), applying the matrix derivative equivalent of (21) to $\ln|\det(\underline{\underline{h}})| \equiv (1/2)\ln[\det(\underline{\underline{h}})\det(\underline{\underline{h}})^*]$ yields after some algebra

$$\frac{\partial \ln|\det(\underline{\underline{h}})|}{\partial \underline{\underline{h}}^*} = \frac{1}{\det(\underline{\underline{h}})^*}\frac{\partial \det(\underline{\underline{h}}^*)}{\partial \underline{\underline{h}}^*} = (\underline{\underline{h}}^\dagger)^{-1} \quad (23)$$

because $\det(\underline{\underline{h}})^* = \det(\underline{\underline{h}}^*) = \det(\underline{\underline{h}}^\dagger)$. The second equality in (23) results from

$$\frac{\partial \det(\underline{\underline{h}}^*)}{\partial \underline{\underline{h}}^*} = \left[\frac{\partial \sum_{n=1}^N h^*_{mn}\mathcal{H}^*_{mn}}{\partial h^*_{mn}}\right] = [\mathcal{H}^*_{mn}] = \mathrm{adj}(\underline{\underline{h}}^\dagger) \quad (24)$$

where $\mathcal{H}_{mn}$ denotes the cofactor of $h_{mn}$ for $\underline{\underline{h}}$. Combining (7), (22), and (23) thus yields

$$\frac{\partial \overline{\ln[L(\underline{\underline{h}})]}}{\partial \underline{\underline{h}}^*} = \overline{\underline{\phi}(\underline{\underline{h}} \cdot \underline{z}_m)\underline{z}_m^\dagger} + (\underline{\underline{h}}^\dagger)^{-1} \quad (25)$$

in which the vector of *score functions* $\phi_n(\cdot)$ of sources $p_n$ is

$$\underline{\phi}(\underline{p}) \equiv [\phi_n(p_n)] \triangleq \left[\frac{2}{f_{P_n,P_n^*}(p_n,p_n^*)}\frac{\partial f_{P_n,P_n^*}(p_n,p_n^*)}{\partial p_n^*}\right]_{n=1}^N. \quad (26)$$

Alternatively, applying the Brandwood transformation $\partial\psi(z, z^*)/\partial z^* = [\partial\psi(x,y)/\partial x + \mathrm{j}\partial\psi(x,y)/\partial y]/2$ for arbitrary $z = x + \mathrm{j}y$ [32], (26) can be rewritten as

$$\underline{\phi} = \left[\frac{1}{f_{P'_n,P''_n}(p'_n,p''_n)} \times \left(\frac{\partial f_{P'_n,P''_n}(p'_n,p''_n)}{\partial p'_n} + \mathrm{j}\frac{\partial f_{P'_n,P''_n}(p'_n,p''_n)}{\partial p''_n}\right)\right]_{n=1}^N \quad (27)$$

which for real-valued $P_n$ reduces to

$$\underline{\phi} = \left[ \frac{1}{f_{P_n}(p_n)} \frac{\partial f_{P_n}(p_n)}{\partial p_n} \right]_{n=1}^{N}. \tag{28}$$

## REFERENCES


[1] J.-R. Regué, M. Ribó, J.-M. Garell, and A. Martin, "A genetic algorithm based method for source identification and far-field radiated emissions prediction from near-field measurements for PCB characterization," *IEEE Trans. Electromagn. Compat.*, vol. 43, no. 4, pp. 520–530, Nov. 2001.

[2] X. Tong, D. W. P. Thomas, A. Nothofer, P. Sewell, and C. Christopoulos, "Modelling electromagnetic emissions from printed circuit boards in closed environments using equivalent dipoles," *IEEE Trans. Electromagn. Compat.*, vol. 52, no. 2, pp. 462–470, May 2010.

[3] W.-J. Zhao, B.-F. Wang, E.-X. Liu, H. B. Park, H. H. Park, E. Song, and E.-P. Li, "An effective and efficient approach for radiated emission prediction based on amplitude-only near-field measurements," *IEEE Trans. Electromagn. Compat.*, vol. 54, no. 5, pp. 1186–1189, Oct. 2012.

[4] L. R. Arnaut and C. S. Obiekezie, "Empirical emission eigenmodes of printed circuit boards," *IEEE Trans. Electromag. Compat.*, Dec. 2013. DOI: 10.1109/TEMC.2013.2292548.

[5] J. A. Stratton, *Electromagnetic Wave Theory*. Section VIII.4. New York, NY, USA: McGraw-Hill, 1941.

[6] A. Zangwill, *Modern Electrodynamics*. Section IV.6. Cambridge, U.K.: Cambridge Univ. Press, 2013.

[7] L. R. Arnaut, "Mode-stirred reverberation chambers: A paradigm for spatio-temporal complexity in dynamic electromagnetic environments," *Wave Motion*, Sep. 2013, to be published. DOI: http://dx.doi.org/10.1016/j.wavemoti.2013.08.007

[8] C. Jutten and J. Hérault, "Blind separation of sources—I. Adaptive algorithm based on neuromimetic architecture," *Sign. Process.*, vol. 24, pp. 1–10, 1991.

[9] P. Comon, "Independent component analysis, a new concept?" *Sign. Process.*, vol. 36, pp. 287–314, 1994.

[10] S.-I. Amari, A. Cichocki, and H. H. Yang, "A new learning algorithm for blind source separation," in *Advances in Neural Information Processing Systems*. vol. 8: MIT Press, 1996, pp. 757–763.

[11] A. Hyvärinen and E. Oja, "Independent component analysis: algorithms and applications," *Neur. Netw.*, vol. 13, pp. 411–430, 2000.

[12] P. Comon and C. Jutten, *Handbook of Blind Source Separation*. New York, NY, USA: Academic, 2010.

[13] J.-F. Cardoso, "High-order contrasts for independent component analysis," *Neur. Comp.*, vol. 11, no. 1, pp. 157–192, 1999.

[14] M. Masugi, N. Hirasawa, R. Kobayashi, K. Tajima, and H. Yamane, "Proposal of a novel EMI diagnostic system using independent component analysis," in *Proc. 20th Int. Zürich Symp. Electromagn. Compat.*, Jan. 12–16, 2009, pp. 417–420.

[15] S. Zhenfei, S. Donglin, D. Fei, F. Duval, and A. Louis, "A novel electromagnetic radiated emission source identification methodology," in *Proc. Asia-Pacific Int. Symp. Electromagn. Compat.*, Beijing, China, Apr. 12–16, 2010, pp. 645–648.

[16] L. R. Arnaut, "Numerical modelling of bianisotropic and complex composite media," in *Proc. 13th Appl. Comput. Electromagn. Symp. ACES*, vol. 2, Monterey, CA, USA, Mar. 1997, vol. 2, pp. 789–795.

[17] L. R. Arnaut, "Recursive de-embedding procedure for computation of mutual coupling between bianisotropic or complex sources and scatterers," *Archiv Elektron. Übertrag.*, vol. 51, no. 1, pp. 1–8, 1998.

[18] L. R. Arnaut and C. S. Obiekezie, "Stochastic analysis of wideband near-field emissions from dipole antennas and integrated circuits," *IEEE Trans. Electromagn. Compat.*, Aug. 2013, to be published. DOI: 10.1109/TEMC.2013.2273737

[19] E. Ollila and V. Koivunen, "Complex ICA using generalized uncorrelating transform," *Sign. Process.*, vol. 89, pp. 365–377, 2009.

[20] A. Hyvärinen, "Fast and robust fixed-point algorithms for independent component analysis," *IEEE Trans. Neur. Netw.*, vol. 10, no. 3, pp. 626–634, May 1999.

[21] A. Cichocki and R. Unbehauen, "Robust neural networks with on-line learning for blind identification and separation of sources," *IEEE Trans. Circuits Syst.*, vol. 43, no. 11, pp. 894–906, 1996.

[22] D. Pham and P. Garat, "Blind sepration of mixtures of independent sources through a quasi-maximum likelihood approach," *IEEE Trans. Sign. Process.*, vol. 45, no. 7, pp. 1712–1725, Jul. 1997.

[23] J.-F. Cardoso and B. Hvam Laheld, "Equivariant adaptive source separation," *IEEE Trans. Sign. Process.*, vol. 44, no. 12, pp. 3017–3030, Dec. 1996.

[24] T. Adalı, H. Li, M. Novey, and J.-F. Cardoso, "Complex ICA using nonlinear functions," *IEEE Trans. Sign. Process.*, vol. 56, no. 9, pp. 4536–4544, Sep. 2008.

[25] S.-I. Amari, "Natural gradient works efficiently in learning," *Neur. Comp.*, vol. 10, no. 2, pp. 251–276, 1998.

[26] L. R. Arnaut, "Sampling distributions of random electromagnetic fields in mesoscopic or dynamical systems," *Phys. Rev. E*, vol. 80, pp. 03661-1–03661-17, Sep. 2009.

[27] T.-W. Lee, M. S. Lewicki, M. Girolami, and T. J. Sejnowski, "Blind source separation of more sources than mixtures using overcomplete representation," *IEEE Sign. Process. Lett.*, vol. 6, no. 5, pp. 87–90, Apr. 1999.

[28] X. Giannakopoulos, J. Karhunen, and E. Oja, "Experimental comparison of neural algorithms for independent component analysis," *Int. J. Neur. Syst.*, vol. 9, no. 2, pp. 651–656, 1999.

[29] A. Hyvärinen, J. Särelä, and R. Vigáro, "Spikes and bumps: Artefacts generated by independent component analysis with insufficient sample size," in *Proc. Int. Workshop Indep. Comp. Anal. Sign. Sep.*, 1999, pp. 425–429.

[30] L. R. Arnaut, "Time-domain versus frequency-domain computation of spatial correlation functions for near-field measurements," in *Proc. Asia-Pacific Symp. EMC*, Melbourne, Australia, May 2013, pp. 53–56.

[31] J. Eriksson, E. Ollila, and V. Koivunen, "Essential statistics and tools for complex random variables," *IEEE Trans. Sign. Process.*, vol. 58, no. 10, pp. 5400–5408, Oct. 2010.

[32] D. H. Brandwood, "A complex gradient operator and its application in adaptive array theory," *IEE Proc. Parts F and H*, vol. 130., no. 1, pp. 11–16, Feb. 1983.


Authors' photographs and biographies not available at the time of publication.